Paper No.
5922

NACE® INTERNATIONAL CORROSION 2015 CONFERENCE & EXPO

Measurement of Wall Shear Stress in Multiphase Flow and Its Effect on Protective $FeCO_3$ Corrosion Product Layer Removal

Wei Li, Yao Xiong, Bruce Brown, Kok Eng Kee, Srdjan Nesic
Institute for Corrosion and Multiphase Technology
Ohio University, Athens, OH 45701
United States

ABSTRACT

Multiphase flow seen in oil and gas lines can be very turbulent and its effect on corrosion has been debated for decades. However, the effect of turbulence and mechanical forces produced by flow on protective corrosion product layers and inhibitor films is not fully understood. Wall shear stress (WSS) is one of the most important parameters used to characterize flow conditions and to assess the influence of flow on corrosion. In the present study, conducted under controlled laboratory conditions, single-phase water flow and a wide range of gas-liquid flow regimes (stratified flow, slug flow and annular mist flow) have been studied in order to accurately measure WSS using a direct floating element WSS measurement probe. These measurements were complemented by visual recordings using a high speed video camera. In addition, atomic force microscopy (AFM) has been used to quantitatively study the force required to remove $FeCO_3$ crystals from a mild steel specimen surface.

The highest WSS measured was of the order of 10^2 Pa in an atmospheric pressure flow systems. AFM measurements indicated that forces of the order of 10^7 Pa would be required to remove an iron carbonate precipitate from a mild steel surface. This is an important finding which indicates that the WSS typically seen in multiphase flow lines is not sufficient to damage $FeCO_3$ layers which could lead to accelerated and localized corrosion.

Keywords: Two-phase flow; wall shear stress measurements; flow loop; slug flow; AFM.

INTRODUCTION

The effect of multiphase flow on internal pipeline corrosion has been debated for decades.[1-5] Flow has been reported to enhance the mass transport of corrosive species from bulk solution to the steel surface.[6-8] However, the effect of mechanical forces produced by the turbulent flow on the corrosion product layers and/or inhibitor films remains unclear. It has often been arbitrarily stated that wall shear stress (WSS) produced by multiphase flow can be very large and can lead to removal of protective corrosion product layers and failure of inhibitor films.[9-11] Despite the fact that the effect of WSS on

corrosion is often debated in the corrosion community, direct WSS measurement in multiphase flow systems is challenging and the few previous existing measurements have been made by using indirect heat/mass transfer techniques based on the Reynolds' analogy.[8,11]

Basic mechanisms and key factors affecting CO_2 corrosion of mild steel are reasonably well understood.[12,13] Iron carbonate ($FeCO_3$), a common CO_2 corrosion product, can form a protective layer on a mild steel substrate.[14-17] However, partial damage of the layer can lead to the development of a galvanic cell and the initiation of severe localized attack.[18] Therefore, understanding the mechanism of $FeCO_3$ removal is of paramount importance. It has been reported that $FeCO_3$ layers can be removed by mechanical forces and/or chemical dissolution.[19-21] For mechanical removal, the stress required to remove an iron carbonate layer has been measured by tensile strength tests. Yang *et al.* reported required values in excess of 10^7 Pa, what is considered to be many magnitudes greater than the WSS found in typical multiphase flow lines.[22] On the other hand, Schmitt *et al.* claimed that "freak waves" in the near wall region of a flow system possibly contain large enough energy to remove $FeCO_3$ layers.[10] One cannot help but wonder whether there really are measurable mechanical forces exerted on the pipe wall in multiphase flow that lead to a such large (and possibly very short lived) local WSS fluctuations. Without an accurate method for WSS determination, this burning question remains unanswered.

The existing measurements of mechanical stresses required to remove $FeCO_3$ layers also bear a large degree of uncertainty. For example, measurements in the paper of Yang *et al.*[22] relate to normal stresses required to detach a protective $FeCO_3$ layers from a steel substrate, which can be very different from the corresponding shear stresses required to do the same. Their measurements were done on a specific type of steel using a very specific procedure to create and detach the $FeCO_3$ layer. Therefore before one can generalize these findings, independent measurements using a different approach need to be made.

In this work, the WSS in flow systems was directly measured using a floating element stress probe. This method relies directly on measuring the shear force exerted by the flow on the floating element flush mounted at the internal pipe wall. By measuring the displacement of the floating element and correlating it to the mechanical force, the WSS can be determined. The previous prototype of this device had several problems as discussed by Winter et al.[23], such as: the effect of misalignment of the element and an effect of temperature on the accuracy of the measurements. In order to cope with these difficulties, several modifications of this device have been implemented recently. In this work, the floating element was combined with optical fiber strain gauges so that the displacement of the element is measured by changes in the optical spectrum of the strain gauges and correlated to the WSS (Figure 1).[24] The circular shaped floating element was set in a 1/4″-80 (6.35 mm-80) threaded cylindrical sensor enclosure. The nominal gap between the edges of floating element and the inner wall of the sensor enclosure was 100 µm. The sensor is designed to work properly when immersed in a fluid. It allows very small WSS determination and solves the problem of temperature compensation by using two fiber-optical strain gauges at opposite sides of the cantilever. The direct WSS measurements in multiphase flow were complemented by high speed video recordings which were synchronized with measurements of WSS.

Furthermore, in this study, direct force measurements required for removal of individual $FeCO_3$ crystals from a mild steel surface were performed by using Atomic Force Microscopy (AFM). AFM is a high resolution technique that can provide surface imaging and force measurement at the nanoscale. AFM has been utilized in the past to study adsorbed inhibitor film structures as well as the forces required for their removal.[25]

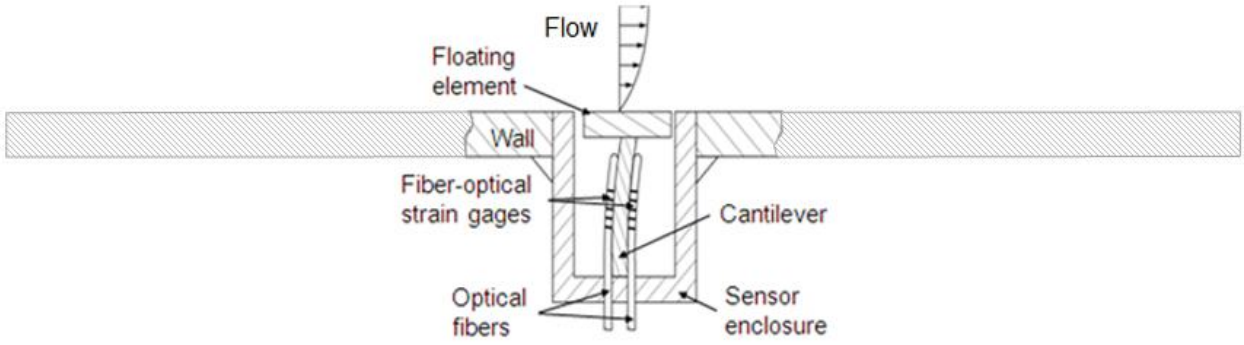

Figure 1: Schematic of a floating element WSS probe connected to an optical fiber strain gauge and flush mounted on the internal pipe wall.[24]

EXPERIMENTAL

Single-Phase Flow Systems

Preliminary experiments were performed in a well-defined single phase flow systems, with the purpose of comparing and validating the direct WSS measurements using a floating element WSS probe with well-established theoretical correlations. Both channel flow and pipe flow have been investigated in separate systems.

For channel flow, a thin channel flow cell system has been used. The schematic for the system and test cell is shown in Figure 2(A). A rectangular cross section test cell (3 mm x 100 mm) which is 600 mm long is shown in Figure 2(B). Four ports can be opened at the bottom plate which allowed plug-in probes such as a differential pressure transducer and the floating element WSS sensor.

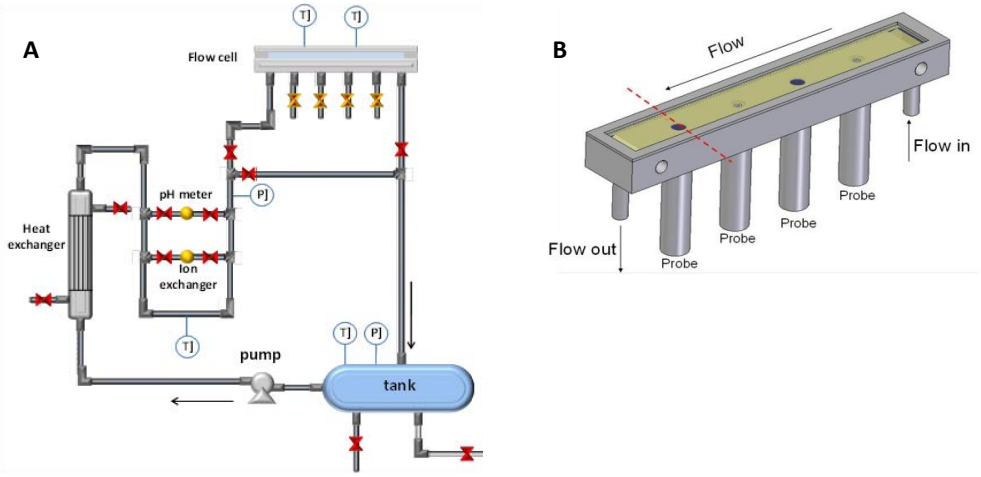

Figure 2: Schematics for: (A) thin channel flow system and (B) rectangular flow cell test section.

For pipe flow, an 1100 liter, 10.1 cm (4 inch) ID pipe horizontal flow loop system has been used (Figure 3). The test section was a transparent acrylic pipe section that allowed flow visualization. The same flow loop system was subsequently used for gas-liquid two-phase flow measurements. Modifications to the WSS probe adaptor were made in the pipe flow study to ensure that the WSS probe was curved and thereby truly flush with the circular cross section profile of the pipe. The test matrix for channel flow and pipe flow experiments is shown in Table 1. The single-phase flow baseline tests provided useful information on the performance of the WSS measurement sensor and laid the groundwork for its

applications in more complicated flow systems such as two-phase or three-phase flow, where accurate WSS predictions are difficult.

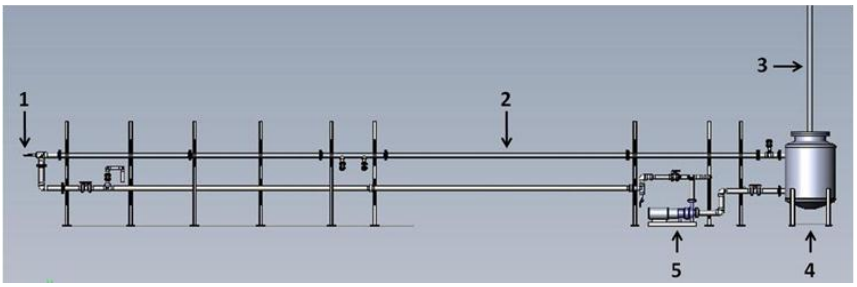

Figure 3: Schematic of an 1100 liter, 10.1 cm ID pipe flow loop.

Table 1.
Test matrices for single phase flow WSS measurements

Parameter	Channel Flow	Pipe Flow
Fluid	DI Water	DI Water
Flow cross section	3mm x 100mm	10.1 cm diameter
Flow velocity	2 m/s – 17 m/s	1 m/s – 2.9 m/s
Pipe material	Stainless steel	PVC pipe
Temperature/pressure	Ambient	Ambient

The correlation between the flow rate and the WSS for single phase flow is well known and is best expressed in terms of non-dimensional parameters: the Reynolds number (Re) and the Fanning friction factor (C_f), which can be found in the literature. The well-known, Patel's[26] correlations (1) and (2), were selected as for friction factor calculation. The WSS was then recovered by using equation (3). These WSS calculations were then compared to the direct WSS measurement by the floating element sensor. The equations are shown below:

Patel's correlation for channel flow:

$$C_f = 0.0376Re^{-1/6} \quad (1)$$

Patel's correlation for pipe flow:

$$C_f = 0.079Re^{-1/4} \quad (2)$$

WSS from the friction factor is calculated as:

$$\tau = \rho\, C_f V^2 / 2 \quad (3)$$

where ρ is fluid density, kg/m^3; V is mean flow velocity, m/s and τ is wall shear stress, Pa.

Gas-Liquid Two-Phase Flow Systems

Experiments of gas-liquid two-phase flow were performed in two horizontal flow systems: a 10.1 cm (4 inch) ID pipe flow loop system and a 15.2 cm (6 inch) ID once-through flow system, as shown schematically in Figure 3 and Figure 4, respectively. The 10.1 cm ID flow loop system can deliver a higher superficial liquid velocity (V_{sl}) range from 0 to 2.9 m/s, while the 15.2 cm ID once-through flow system has a broader superficial gas velocity (V_{sg}) up to 60 m/s, but a narrow V_{sl} range. With the two flow systems, a wide range of horizontal two-phase flow regimes can be investigated. The flow system conditions are shown in Table 2.

The floating element sensor by Lenterra† was employed as the direct *in-situ* WSS measurement in both flow systems. Simultaneously, a high speed camera was employed for flow visualization so that the data can be correlated with the WSS data. The typical video recording rate in this study is 5000 fps (frames per second).

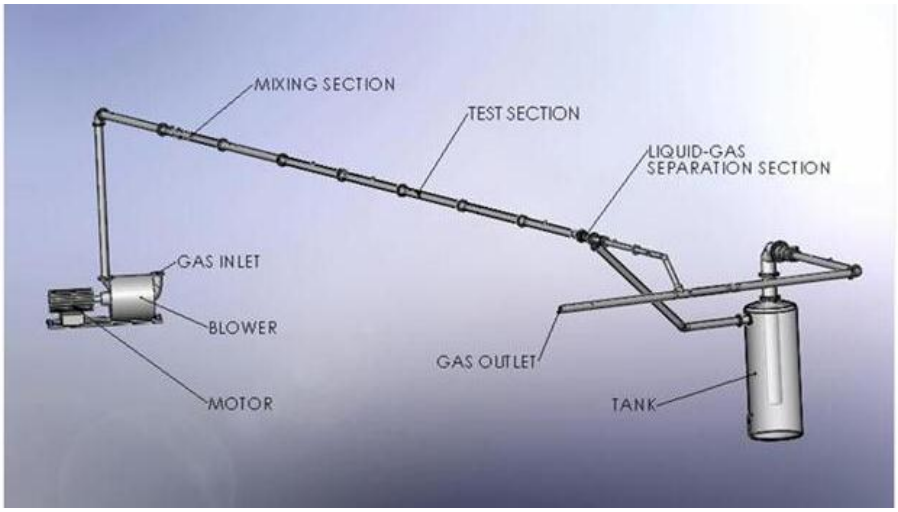

Figure 4: Schematic of 15.2 cm ID once-through pipe system

Table 2.
Flow system conditions for gas-liquid two-phase flow WSS measurements

Parameter	10.1 cm ID flow loop	15.2 cm ID once-through
Liquid	Tap water	Tap water
Gas	CO_2	Air
Superficial liquid velocity range	0 m/s - 2.9 m/s	0 m/s - 0.17 m/s
Superficial gas velocity range	0 m/s - 8 m/s	0 m/s - 60 m/s
Pipe Material	PVC pipe	PVC pipe
Temperature/pressure	Ambient	Ambient

A wide range of flow patterns can exist for two-phase flow in a pipe and, in most of these, the phases are not homogeneously distributed in the pipe cross section. Thus, it is necessary to measure the WSS circumferentially around the pipe. In this part of the project, three locations at the pipe wall were selected: bottom (6 o'clock position), top (12 o'clock position) and side (3 o'clock position). The summary of two-phase flow conditions for which data was collected at the three different positions is shown in the flow regime map in Figure 5. The data points represent measurements which are overlaid with predicted flow regime transition lines provided by MULTICORP 5.0†.

† Trade Name
† Trade name.

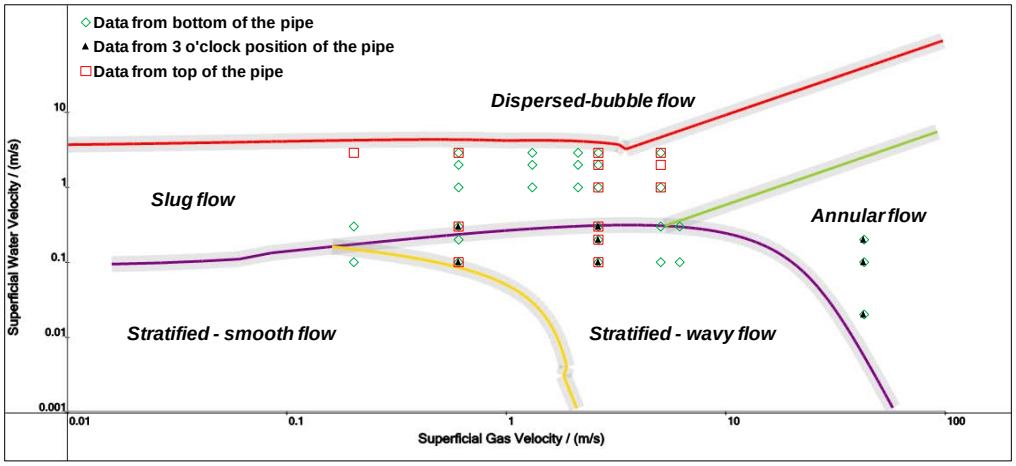

Figure 5: Two-phase flow regime map with conditions used in the analysis of WSS for the three different positions around the pipe

AFM Study of Removal of $FeCO_3$ Crystals from a Mild Steel Surface

$FeCO_3$ crystals were formed in a 2 liter glass cell at the condition listed in Table 3. The details of sample preparation can be found elsewhere.[27] After the test, SEM analysis was carried out to confirm the morphology of the $FeCO_3$ crystals. Figure 6 shows the SEM images of $FeCO_3$ crystals formed on the X65 steel specimen. Isolated crystals were developed for further AFM imaging. The basic principles of AFM operation and imaging can be found elsewhere.[25]

Table 3.
Conditions for developing $FeCO_3$ layer in a 2 L glass cell

Test solution	DI Water,1 wt % NaCl, 50 ppm Fe^{2+}
Temperature	80 °C
Partial Pressure of CO_2	0.526 bar at 80 °C
pH	6.6
Test material	X65 carbon steel, (Polished with 400 grit, 600 grit, 1500 grit, then with 320 silk cloth with 9 µm diamond suspension.)
Test duration	20 hrs

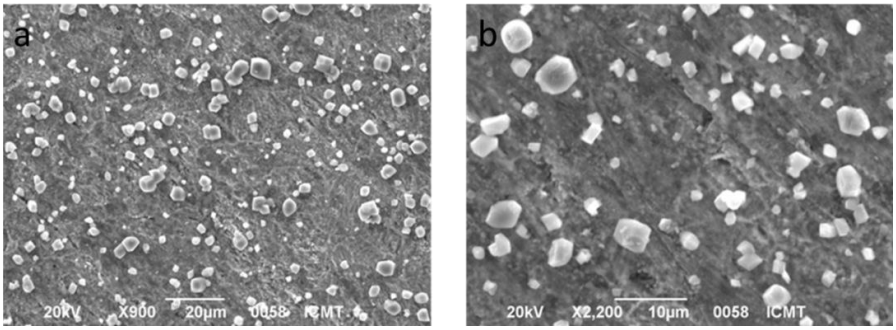

Figure 6: SEM images of $FeCO_3$ crystals on X65 steel specimen at various magnifications.

The $FeCO_3$ crystals were then imaged and removed from the steel surface by the AFM tip using a three-step procedure, shown in Figure 7. In the first step, topography images were collected on the area where $FeCO_3$ crystals formed. For those topography images, a low normal force (< 2 µN) was

applied to provide a necessary load for imaging but also to avoid damaging the $FeCO_3$ crystals. In the second step, the normal force applied to the cantilever was gradually increased to remove the $FeCO_3$ crystals. The force values were recorded when $FeCO_3$ crystals were removed. In the last step, topography images were collected on the exactly same area where $FeCO_3$ crystals were removed, by applying a low normal force again. Here, it should be emphasized that this normal force, applied in vertical direction (normal to the steel surface), is not the force causing the removal of the $FeCO_3$ crystals. This applied normal force is related to a lateral force in the horizontal direction which is responsible for the direct interaction between the scanning probe tip and the $FeCO_3$ crystals. Therefore, the normal force was first measured and then the lateral force leading to the removal of $FeCO_3$ crystals was calculated.[25]

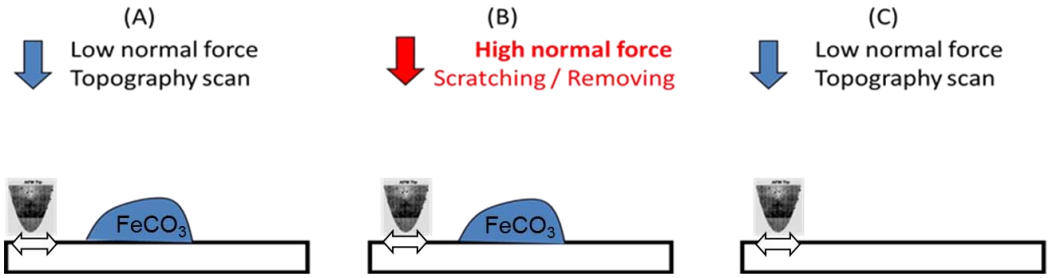

Figure 7: A three-step procedure for imaging and removing $FeCO_3$ crystals from the steel surface.

RESULTS AND DISCUSSION

WSS Measurements in Single-Phase Flow

The results obtained by the floating element sensor and the Patel's correlation for single phase channel and pipe flows are compared in Figure 8 and Figure 9, respectively. It can be seen that the mean WSS measured by the floating element sensor in channel flow (Figure 8) shows a reasonably good agreement with Patel's correlation (1) over a large range of flow rates. In addition, the results from single phase pipe flow (Figure 9) were also compared to the Patel's correlation (2). From this graph, it can be seen that the floating element measurement is consistent with the predictions made by Patel's correlation as well. One can conclude that the floating element method worked reasonably well as the result shows a good agreement with the well-known single-phase WSS correlations for both channel flow and pipe flow.

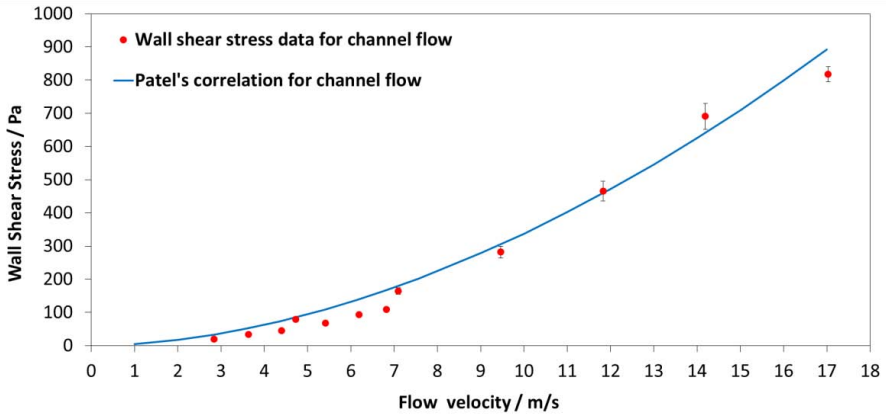

Figure 8: Comparison of WSS values obtained by Patel's correlation (1) to direct measurement made by using a floating element sensor in single-phase channel flow.

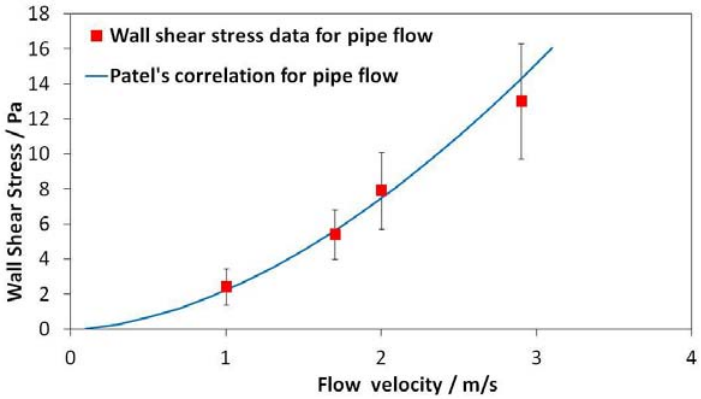

Figure 9: Comparison of WSS values obtained by Patel's correlation (2) to direct measurement made by using a floating element sensor in single-phase pipe flow.

WSS Measurements in Gas-Liquid Two-Phase Horizontal Pipe Flow

The successful application of the floating element WSS sensor in single phase flow raised the confidence about application in multiphase flow WSS determination, where the flow environment is much more complicated and far less understood. Since no well-established WSS correlations could be found for multiphase flow, direct WSS measurements provide vital information for such a purpose. In the following section, the application of floating element WSS sensor in two-phase flow is discussed. Three locations: bottom, side and top of the pipe, have been investigated.

Wall Shear Stress Measurements at Bottom of the Pipe (6 o'clock Position).

A maximum WSS value measured at the bottom of the pipe in each condition is entered into a corresponding flow regime map (see Figure 10). It clearly shows that with increasing V_{sl} and V_{sg}, there is a trend of increasing maximum WSS (diagonally from lower left to upper right). It was also found that in the slug flow regime, the slug frequency (slugs/second) increased with the increasing V_{sl} and V_{sg}.

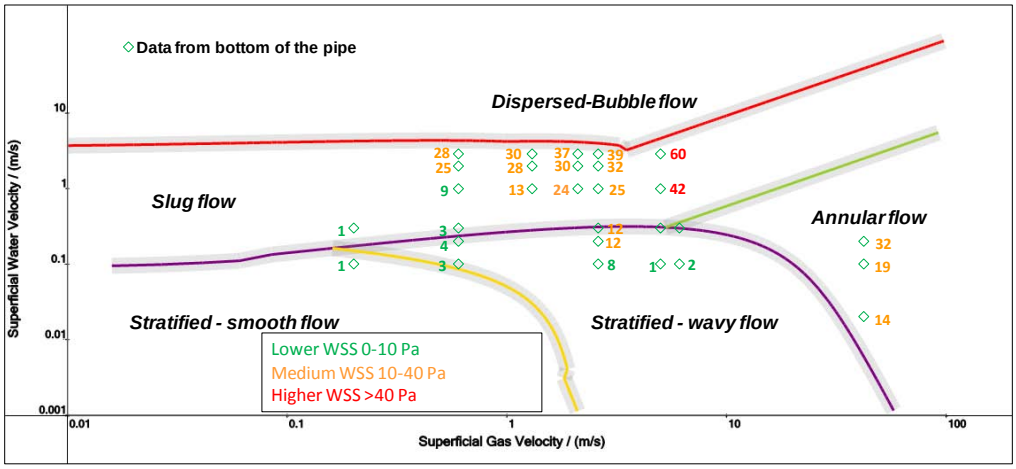

Figure 10: Two-phase flow regime map with τ_{max} (Pa) plotted at 1bar (100 kPa) CO_2, 25 ^oC, in a 10.1 cm and a 15.2 cm ID pipe, WSS probe is at the bottom of the pipe.

In order to investigate the relationship between the WSS measurement and the flow regimes, a synchronized high speed camera was used in tandem with a floating element sensor. The tests at V_{sl} = 2.0 m/s and V_{sg} = 2.1 m/s were used to illustrate the evolution of *in-situ* WSS measurement in a slug flow regime. The evolution of WSS measurement for the slug flow condition is shown in Figure 11(A).

The measurement peaks indicate the slug passage, as confirmed by the high speed camera recordings. Figure 11(B) shows an enlarged portion between the red dotted lines in Figure 11(A), where the measurement peaks can be seen more clearly. Figure 12 presents the flow visualization of a passing slug corresponding to a WSS peak highlighted by a red circle in Figure 11 (B). In this test, the highest WSS occurred exactly when the slug front passed the WSS probe location. However, this was not necessarily the case for all other slug flow conditions. For example, Figure 13 shows one WSS peak with the corresponding slug image for V_{sl} = 2.9 m/s and V_{sg} = 5.0 m/s.

Wall Shear Stress Measurements on Top of the Pipe (12 o'clock Position).

Figure 14 shows the maximum WSS value measured when the probe was at the top of the pipe. Generally, as was observed for WSS measurements at the bottom of the pipe, when the V_{sg} and V_{sl} were increased, the slug frequency increased, and the measured maximum WSS increased. Furthermore, maximum WSS at the top of the pipe was of higher magnitude than maximum WSS under the same test conditions when the probe was at bottom of the pipe. For instance, when the V_{sl} = 0.3 m/s and V_{sg} = 2.6 m/s, the maximum WSS is 49 Pa at top whilst it is 12 Pa at bottom. In addition, the WSS measurement peaks were more distinctive and the fluctuations of WSS were more severe. When compared to the flow visualization data, it is confirmed that the peak values indicate slug occurrences. Figure 15 shows one measurement peak indicated by a red circle with the corresponding slug image at V_{sl} = 2.9 m/s and V_{sg} = 5.0 m/s. In this test, the highest WSS occurred soon after the slug front passed the WSS probe. Similarly, in other tests in the slug flow regime, it was found the highest WSS always occurred as the slug was passing the probe. Flow velocity analysis from the high speed camera images confirmed that the top of the slug front had the largest velocity which was approximately equal to V_{sl} + V_{sg}. This is consistent with a much higher WSS found at the top of the pipe.

Wall Shear Stress Measurements on the Side Wall of the Pipe (3 o'clock Position).

The maximum WSS data collected by the WSS sensor mounted at the 3 o'clock position is shown in Figure 16. A similar trend was also observed that increasing V_{sg} and V_{sl} would lead to a higher maximum WSS in each individual flow regime. Generally, the maximum WSS measured was not as large as the maximum WSS measured at the top of the pipe under the same conditions. However, they were higher than those measured at the bottom of the pipe.

The subsequent section will examine if these WSS measured in single and two-phase flow correspond in magnitude to the forces required to remove crystals of protective $FeCO_3$ from a mild steel surface, as measured by AFM.

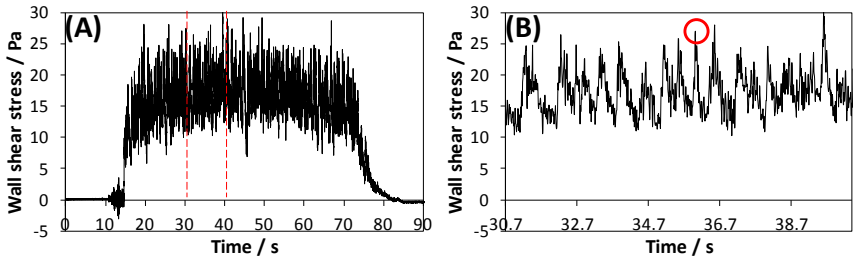

Figure 11: Wall shear stress measurement at bottom of the 10.1 cm ID pipe for V_{sl} =2.0 m/s, V_{sg} = 2.1 m/s: (A) full measurement sequence; (B) zoom between 30 and 40 seconds.

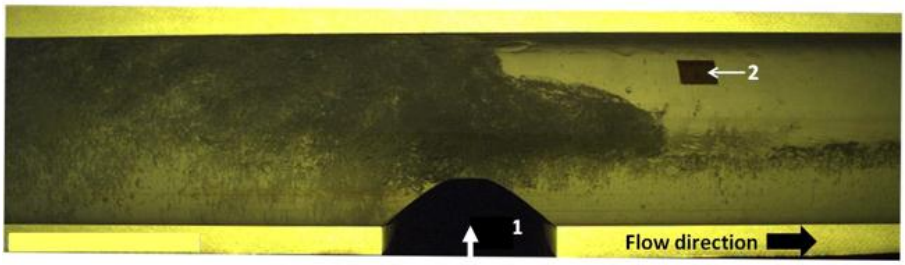

Figure 12: Image of slug passage; V_{sl} = 2.0 m/s, V_{sg} = 2.1 m/s, corresponding to the red circled WSS measurement data point in Figure 11(B): 1. WSS probe location at the pipe bottom; 2. scale tape of 2 cm in length.

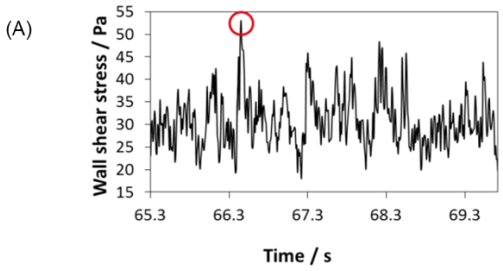

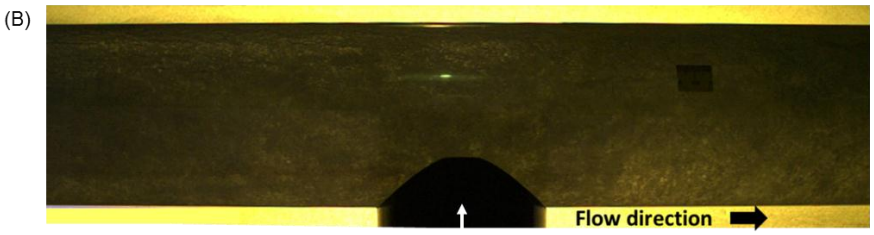

Figure 13: (A) Wall shear stress measurement at bottom of the 10.1 cm ID pipe for V_{sl} = 2.9 m/s, V_{sg}= 5.0 m/s. (B) Image of slug passage corresponding to the red circled WSS measurement data point in (A).

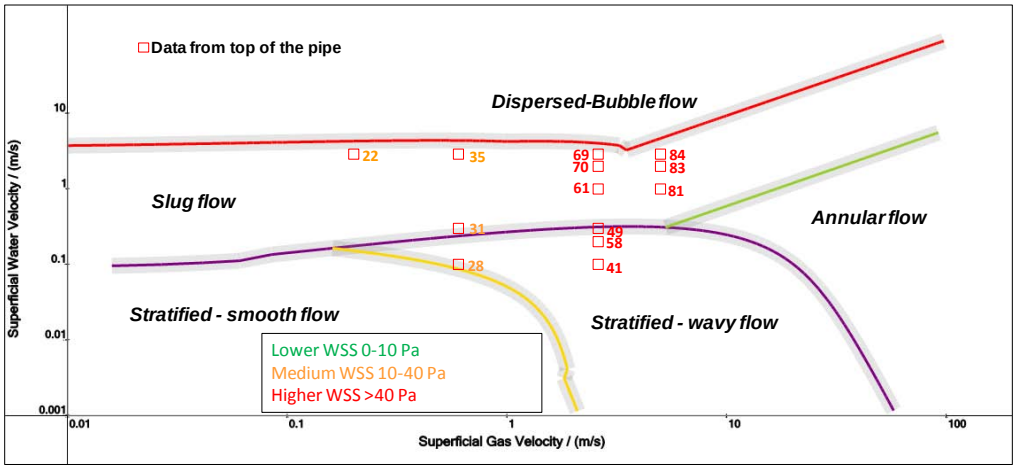

Figure 14: Two-phase flow regime map with τ_{max} (Pa) plotted at 1bar (100 kPa) CO_2, 25 ^oC, in a 10.1 cm and a 15.2 cm ID pipe, WSS probe is at top of the pipe.

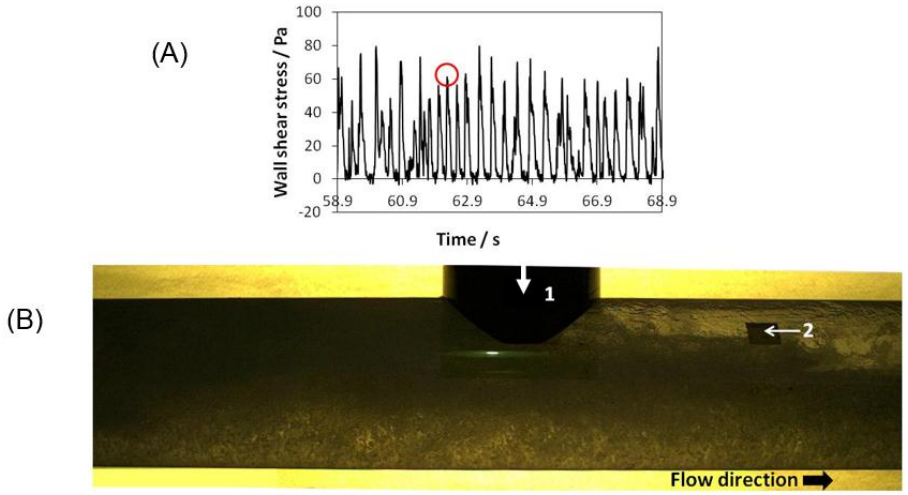

Figure 15: (A) Wall shear stress measurement at top of the 10.1 cm ID pipe for V_{sl} =2.9 m/s, V_{sg} = 5.0 m/s, slug flow. (B) Image of slug passage corresponding to the red circled WSS measurement data point in (A). 1. WSS probe location flush mounted at the pipe top; 2. scale tape of 2 cm in length.

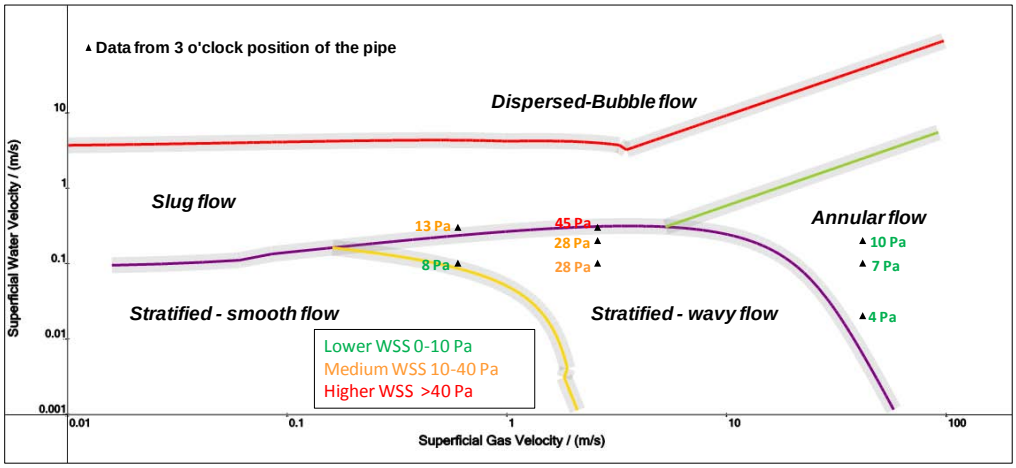

Figure 16: Two-phase flow regime map with τ_{max} (Pa) plotted at 1bar (100 KPa) CO_2, 25 ^oC, in a 10.1 cm and a 15.2 cm ID pipe, WSS probe is at side of the pipe.

Force Calculation for Removal of $FeCO_3$ Crystals from Mild Steel Surface

Removal of $FeCO_3$ Crystals and Normal Force Measurements.

Figure 17a shows the topography images of a 30 µm × 30 µm area on the sample surface. In Figure 17a, four $FeCO_3$ crystals are numbered, shown as white features. Their width and length are approximately 5 to 10 µm, which are consistent with the dimensions of $FeCO_3$ shown in SEM images (see Figure 6). AFM measurements suggest that the height of $FeCO_3$ crystals is approximately 2 to 3 µm, which is significantly larger than the measured steel surface roughness (200 nm). Therefore, individual $FeCO_3$ crystals could be detected by the AFM scanning probe.

At the beginning of the test, the four $FeCO_3$ crystals were imaged by using a low normal force of 1.4 µN (Figure 17a). Crystal no.2 was first removed by increasing the applied normal force to 8.4 µN (Figure 17b), while the other three crystals resisted this force. When the force reached 22 µN, crystals no.1 and no.3 were removed by the probe (Figure 17d). Crystal no.4 was still intact even after applying a

maximum normal force of 30 µN. Further analysis was carried out on the other areas of this sample until a total of 9 $FeCO_3$ crystals were removed using this 3-step procedure. The normal force values were from 0.7 µN to 25 µN. This indicates that the adhesion force between the $FeCO_3$ crystals and steel surface varies at least one order of magnitude and is expected to be dependent on the size, shape, and surface contact area of each crystal. Since the height and shape of these $FeCO_3$ crystals was similar, the dominant factor affecting the adhesion of crystals was most likely the contact area. Figure 18 shows the applied normal forces to remove $FeCO_3$ crystals vs. cross-section areas. Cross-section areas of crystals were directly measured from topography images (Figure 17). From this figure, it was found that the normal forces leading to the removal of crystals were related to the cross-section area of crystals. Larger crystals exhibited higher adhesion and required higher removal forces.

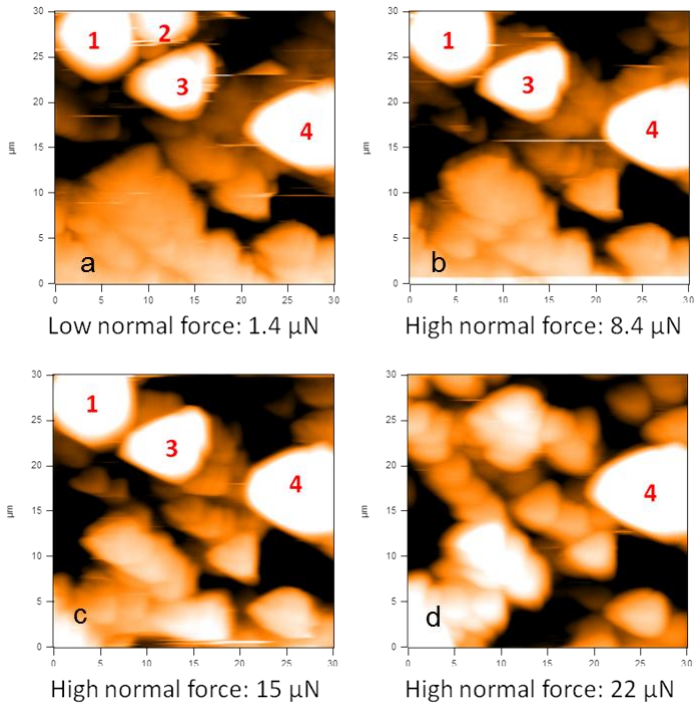

Figure 17: AFM topography images of four $FeCO_3$ crystals scanned by applying different normal force:(a) 1.4 µN, (b) 8.4 µN, crystal no.2 is removed (c) 15 µN, (d) 22 µN, crystals no. 1 and no. 3 are removed during the scanning. Crystal no.4 cannot be removed by applying 30 µN which is the maximum value instrument can provide.

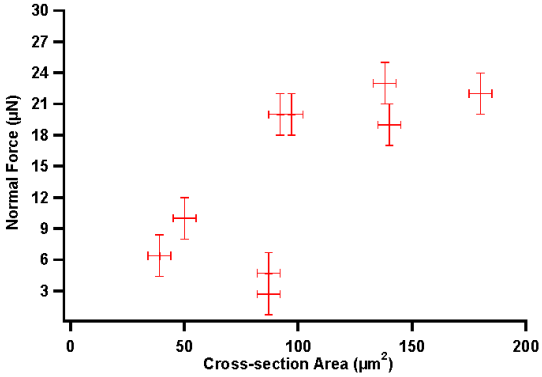

Figure 18: Applied normal forces to remove $FeCO_3$ vs. cross-section area.

Calculation of Lateral Force and Corresponding Stress for Removal of $FeCO_3$ Crystals.

In the above section, the description of the normal forces leading to the removal of $FeCO_3$ was given. The normal force, however, is not a measure of the direct interaction between the scanning probe and the crystal. A calculation of lateral force which is the actual force responsible for removing $FeCO_3$ crystals is required. In order to convert the normal force measurements to lateral force values, an AFM parameter called lateral spring constant is used. In this study, lateral spring constant of 980 ± 80 N/m for the diamond tip was calculated by using the method reported in the literature.[28] The details of how to convert the normal force data into the lateral force values can be found elsewhere.[25] Figure 19 shows the measured lateral force at various applied normal force conditions. From this graph, it can be seen that the lateral force is directly proportional to the applied normal force. Therefore, the measured normal force leading to the removal of $FeCO_3$ crystal (Figure 18) can be converted to the lateral force (Figure 19). Further considering the area of crystals, the lateral stress values can be calculated, as shown in Table 4. The calculation reveals that the lateral stress values for removing the nine crystals varies from 0.7 MPa to 17 MPa. Considering the possible error from the use of cross-section area which is smaller than the real contact area, we can estimate that the lateral stress values are of the order of 0.1 to 10 MPa.

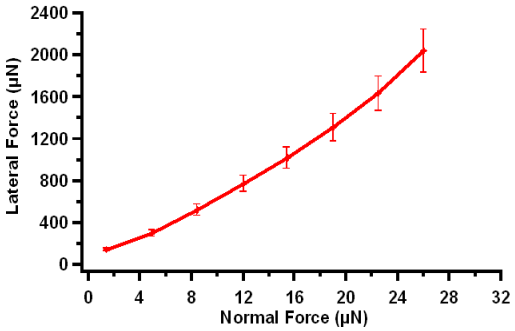

Figure 19: Lateral force vs normal force graph. The lateral forces were calculated by applying different normal forces.

Table 4.
Normal force, lateral force, cross-section area and stress values for removal of the nine $FeCO_3$ crystals.

No.	Normal force (μN)	Lateral force (μN)	Area (μm^2)	Stress (MPa)
1	21	1526	140	11
2	24	1755	180	10
3	0.7	51	87	0.6
4	4.7	283	87	3
5	8.4	565	39	14
6	22	1602	92	17
7	22	1602	97	16
8	25	1831	138	13
9	12	840	50	17

Discussion

Based on the results for single-phase and two-phase flow WSS measurements, the floating element sensor method was successfully used to measure WSS. It was found that in the slug flow regime, which is considered to be one of the most violent multiphase flow regimes, the highest WSS occurs on the top of the pipe when the slug passes. It is speculated that the water layer at the bottom of the pipe

in slug flow regime can dampen the impact of the slugs. Therefore, a much smaller WSS value is found at the bottom of the pipe when the slug passes. In this study, for ambient pressure horizontal gas-liquid two-phase flow, the highest WSS recorded was approximately 10^2 Pa in magnitude.

According to the AFM measurement, the calculated lateral stress required to remove $FeCO_3$ crystals is of at least 10^6 Pa magnitude, which is in broad agreement with measurements reported by Yang *et al.*[22] using tensile tests. There is a large gap between the required stress to remove $FeCO_3$ crystals and what is seen in realistic multiphase flow. Even if one accounts for more extreme flow conditions seen in larger pipes at higher pressure and gas densities, it is still difficult to imagine that the difference which is at least 3-4 orders of magnitude can be reconciled. This indicates that the removal of $FeCO_3$ layer solely by WSS exerted by fluid flow is unlikely. Clearly one must search for other explanations.

CONCLUSIONS

Several conclusions can be drawn:

- The floating element provides a new effective way to directly measure WSS in multiphase flow.
- The direct WSS measurements made by using the floating element sensor have been verified with Patel's correlation for single phase pipe flow and channel flow.
- The highest WSS in a horizontal gas-liquid two-phase slug flow regime occurs on the top section of the pipe wall when the slug front passes.
- Flow visualization was used to confirm that the peaks in the WSS measurement data can be used to measure slug frequency.
- In the tested flow conditions at atmospheric pressure, the maximum WSS for any flow regime was less than 10^2 Pa in magnitude.
- According to stress calculations using AFM force measurements, the lateral stress required to remove $FeCO_3$ crystals from a steel surface is of a 10^6 Pa order of magnitude.
- This suggests that the mechanical removal of an $FeCO_3$ layer solely by WSS typically seen in multiphase flow lines is highly unlikely and that other factors need to be considered.

ACKNOWLEDGEMENTS

The authors would like to acknowledge the financial support from the following companies: Anadarko, Baker Hughes, BP, Chevron, Clariant Oil Services, CNPC Tubular Goods Research Center, ConocoPhillips, DNV USA, Inc., Hess, INPEX Corporation, M-I SWACO, Multi-Chem, Nalco Champion, Occidental Oil Company, Petrobras, Petroleum Development Oman, Petroleum Institute (Gas Research Center), Petronas, PTT, Saudi Aramco, SINOPEC, TransCanada, TOTAL, Wood Group Integrity Management. Discussion with Dr. B.F.M. Pots is greatly appreciated.

REFERENCES

1. A.S. Green, B.V. Johnson, H.J. Choi, "Flow-Related Corrosion in Large-Diameter Multiphase Flowlines," *SPE Prod. Facil.* 8 (1993): p. 97-100.
2. L. Jiang, M. Gopal, "Multiphase Flow-Enhanced Corrosion Mechanisms in Horizontal Pipelines," *J. Energy Resour. Technol.* 120 (1998): p. 67-71.
3. J. K. Heuer, J. F. Stubbins, "Microstructure Analysis of Coupons Exposed to Carbon Dioxide Corrosion in Multiphase Flow," *Corrosion* 54 (1998): p. 566-575.
4. B. Heeg, T. Moros, D. Klenerman, "Persistency of Corrosion Inhibitor Films on C-Steel under Multiphase Flow Conditions. Part I: the Jet-Cylinder Arrangement," *Corros. Sci.* 40 (1998): p. 1303-1311.
5. Y. Chen, T. Hong, M. Gopal, W.P. Jepson, "EIS Studies of a Corrosion Inhibitor Behavior under Multiphase Flow Conditions," *Corros. Sci.* 42 (2000): p. 979-990.
6. A. Demoz, T. Dabros, "Relationship between Shear Stress on the Walls of a Pipe and an Impinging Jet," *Corros. Sci.* 50 (2008): p. 3241–3246.

7. K.D. Efird, E.J. Wright, J.A. Boros, T.G. Hailey, “Correlation of Steel Corrosion in Pipe Flow with Jet Impingement and Rotating Cylinder Tests,” *Corrosion* 49 (1993): p. 992–1003.
8. H. Wang, T. Hong, J. Cai, H.D. Dewald, W.P. Jepson, “Enhancement of the Instantaneous Mass - Transfer Coefficient in Large Diameter Pipeline under Water/Oil Flow,” *J. Electrochem. Soc.* 147 (2000): p. 2552–2555.
9. G. Schmitt, M. Mueller, "Critical Wall Shear Stresses in CO_2 Corrosion of Carbon Steel," CORROSION/99*,* paper no.44 (Houston, TX: NACE, 1999).
10. R.H. Hausler, G. Schmitt, “Hydrodynamic and Flow Effects on Corrosion Inhibition,” CORROSION/2004, paper no.04402 (Houston, TX: NACE, 2004).
11. G. Schmitt, C. Werner, M. Bakalli, “Fluid Mechanical Interactions of Turbulent Flowing Liquids with the Wall-Revisited with a New Electrochemical Tool,” CORROSION/2005, paper no. 05344 (Houston, TX: NACE, 2005).
12. S. Nesic, “Carbon Dioxide Corrosion of Mild Steel”, in *Uhlig’s Corrosion Handbook*, 3rd ed., eds. R. Winston Revie (Hoboken, New Jersey: John Wiley & Sons, Inc., 2011), p. 229-245.
13. S. Nesic, W. Sun, “Corrosion in Acid Gas Solutions”, in *Shreir’s Corrosion*, eds. J. A. Richardson, et al. (Amsterdam, The Netherlands: Elsevier, 2010), p. 1270-1298.
14. W. Sun, S. Nesic, R.C. Woollam, "The Effect of Temperature and Ionic Strength on Iron Carbonate ($FeCO_3$) Solubility Limit," *Corros. Sci.* 51 (2009): p. 1273-1276.
15. T. Li, Y. Yang, K. Gao, M. Lu, "Mechanism of Protective Film Formation During CO_2 Corrosion of X65 Pipeline Steel," *J. Univ. Sci. Technol. B.* 15 (2008): p. 702-706.
16. C. Ding, K. Gao, C. Chen, "Effect of Ca^{2+} on CO_2 Corrosion Properties of X65 Pipeline Steel," *Int. J. Min. Met. Mater.* 16 (2009): p. 661-666.
17. J. Zhang, Z.L. Wang, Z.M. Wang, X. Han, "Chemical Analysis of the Initial Corrosion Layer on Pipeline Steels in Simulated CO_2-Enhanced Oil Recovery Brines," *Corros. Sci.* 65 (2012): p. 397-404.
18. J. Han, D. Young, H. Colijn, A. Tripathi, S. Nesic, "Chemistry and Structure of the Passive Film on Mild Steel in CO_2 Corrosion Environments," *Ind. Eng. Chem. Res.* 48 (2009): p. 6296-6302.
19. S. Nesic, K. L. J. Lee, “A Mechanistic Model for Carbon Dioxide Corrosion of Mild Steel in the Presence of Protective Iron Carbonate Films - Part 3: Film Growth Model,” *Corrosion* 59 (2003): p.616-628.
20. V. Ruzic, M. Veidt, S. Nesic, “Protective Iron Carbonate Films—Part 1: Mechanical Removal in Single-Phase Aqueous Flow. Corrosion,” *Corrosion* 62 (2006): p.419-432.
21. V. Ruzic, M. Veidt, S. Nesic, “Protective Iron Carbonate Films—Part 2: Chemical Removal by Dissolution in Single-Phase Aqueous Flow,” *Corrosion* 62 (2006): p.598-611.
22. Y. Yang, B. Brown, S. Nesic, M. Elena Gennaro, B. Molinas, “Mechanical Strength and Removal of a Protective Iron Carbonate Layer Formed on Mild Steel in CO_2 Corrosion,” CORROSION/2010, paper no. 10383 (Houston, TX: NACE, 2010).
23. K. G. Winter, “An Outline of the Techniques Available for the Measurement of Skin Friction in Turbulent Boundary Layers,” *Prog. Aerospace Sci.* 18 (1979): p. 1-57.
24. V. Sheverev, B. Brown, S. Nesic, “Direct Measurement of Wall Shear Stress in Single - and Multiphase Flows,” Internet: http://www.lenterra.com/downloads/, [Aug. 20, 2013].
25. Y. Xiong, B. Brown, B. Kinsella, S. Nesic, A. Pailleret, “Atomic Force Microscopy Study of the Adsorption of Surfactant Corrosion Inhibitor Films,” *Corrosion* 70 (2014): p. 247-260.
26. V.C. Patel, “Some Observations on Skin Friction and Velocity Profiles in Fully Developed Pipe and Channel Flows,” *J. Fluid Mech.* 38 (1969): p. 181-201.
27. W. Li, B. Brown, D. Young, S. Nesic, “Investigation of Pseudo-Passivation of Mild Steel in CO_2 Corrosion,” *Corrosion* 70 (2014): p. 294-302.
28. Y. H. Liu, T. Wu, D. F. Evans, “Lateral Force Microscopy Study on the Shear Properties of Self-Assembled Monolayers of Dialkylammonium Surfactant on Mica,” *Langmuir* 10 (1994): p. 2241-2245.